Journal of
Applied Crystallography
ISSN 0021-8898

Received 22 December 2006
Accepted 12 July 2007

Threading dislocations in domain-matching epitaxial films of ZnO

W.-R. Liu,[a] W. F. Hsieh,[a] C.-H. Hsu,[b,a]* Keng S. Liang[a] and F. S.-S. Chien[c]

[a]Department of Photonics and Institute of Electro-Optical Engineering, National Chiao Tung University, Hsinchu 300, Taiwan, [b]National Synchrotron Radiation Research Center, Hsinchu 300, Taiwan, and [c]Department of Physics, Tunghai University, Taichung 407, Taiwan. Correspondence e-mail: chsu@nsrrc.org.tw

The structures of high-quality ZnO epitaxial films grown by pulsed-laser deposition on sapphire (0001) without an oxygen gas flow were investigated by X-ray diffraction and transmission electron microscopy. The great disparity of X-ray diffraction line widths between the normal and in-plane reflections reveals the specific threading dislocation geometry of ZnO. Most threading dislocations are pure edge dislocations. From a combination of scattering and microscopic results, it is found that threading dislocations are not uniformly distributed in the ZnO films, but the films consist of columnar epitaxial cores surrounded by annular regions of edge threading dislocations in large density. The local surface morphology and capacitance signal obtained from atomic force and scanning capacitance microscopes indicate that the aggregation of threading dislocations leads to high interface traps at the annular regions.

1. Introduction

Wurtzite ZnO, a II–VI semiconductor with a large direct band gap (3.37 eV), has been intensively investigated because of a strong commercial demand for emitters of blue and UV light. An attractive feature of ZnO is its large exciton binding energy, 60 meV, which is about three times that of GaN or ZnSe (Bagnall *et al.*, 1997). ZnO has thus great thermal stability for excitons and offers a good prospect for practical lasers with small thresholds even at high temperatures.

Two critical factors that govern the quality of hetero-epitaxial films are the mismatches of lattice parameters and thermal expansion coefficients between the deposited layer and substrate. ZnO has a wurtzite structure with a = 3.25 Å and c = 5.21 Å, and sapphire (α-Al_2O_3), the most commonly used substrate for ZnO growth, has a rhombohedral crystal structure with a = 4.76 Å and c = 12.99 Å. In view of the significant differences in structure and lattice parameters, it has been a challenge to grow high-quality ZnO epitaxial films on sapphire. Narayan & Larson (2003) proposed that ZnO films can be grown on a c-plane sapphire substrate by domain-matching epitaxy (DME) in the initial stage of growth. The matching of five or six $(21\bar{1}0)$ planes of ZnO with six or seven $(30\bar{3}0)$ planes of sapphire leads to a rotation of the ZnO epilayer by 30° against the c plane of the sapphire substrate, and thus the lattice mismatch decreased from 32 to 18%. The distinct thermal expansion coefficient of ZnO and sapphire introduces an additional strain upon post-growth cooling (Vigué *et al.*, 2001). To accommodate such a large lattice mismatch, the strain energy must be released through the generation of various defects in the epitaxial films. The type and geometry of these defects play a crucial role in determining the mechanical, electrical and optical properties of the films.

For GaN thin films, which have the same wurtzite crystal structure as ZnO, the characteristic defects are high-density, typically 10^9–10^{11} cm^{-2}, threading dislocations (TDs) with the dislocation lines penetrating throughout the entire film. TDs affect the electrical and optical properties of films, including the degradation of devices through carrier scattering (Ng *et al.*, 1998), nonradiative recombination (Sugahara *et al.*, 1998) and a reverse-bias leakage current (Hsu *et al.*, 2002; Miller *et al.*, 2002). Therefore, to understand and subsequently to improve effectively the physical properties of ZnO thin films, a thorough structural investigation of the characteristics of defects in ZnO epi-films is warranted.

X-ray diffraction (XRD) is well established for quantitative exploration of the defect structure over a macroscopic length scale in accordance with crystal imperfection (Krivoglaz, 1996). Transmission electron microscopy (TEM) is another powerful technique to characterize the local defect structure and provides structural information complementary to what we can learn from XRD. Scanning capacitance microscopy (SCM), an extension and variant of atomic force microscopy (AFM), measures the local capacitance of the metal oxide semiconductor structure formed by a metallic coated tip and a semiconductor sample. SCM records the variation of capacitance as a function of applied voltage, dC/dV, which originates from the carrier motion in the semiconductor in response to a low-frequency AC electrical modulation (V_{ac}) superimposed on a DC tip bias (V_{tip}) between the sample and tip. By scanning the tip across the sample surface, the lateral variation of

the carrier density and carrier type with nanometre resolution together with surface morphology are probed simultaneously (Hansen *et al.*, 1998).

In this article, we report a comprehensive study of the structural properties of the ZnO epitaxial layers grown by pulsed-laser deposition (PLD) on (0001) sapphire substrates, including heterogeneous strain, correlation length, tilt and twist angles, and the density of TDs. Cross-sectional TEM was conducted to identify the type and density of the TDs; XRD was carried out to perform quantitative structural analysis. To correlate the surface morphology with the distribution of TDs and to characterize the influence of the TDs on the electric properties at the microscopic scale, we have also conducted AFM and SCM measurements.

2. Experimental

The ZnO films were grown on (0001) sapphire substrates by PLD, which is commonly adopted for the growth of ZnO epifilms (Tsukazaki *et al.*, 2005). The beam of a KrF excimer laser ($\lambda = 248$ nm) was focused to produce an energy density of ~5–7 J cm^{-2} at a repetition rate of 10 Hz on a commercial hot-pressed stoichiometric ZnO (99.99% purity) target. The films were deposited with a growth rate of ~0.625 Å s^{-1} at a substrate temperature of 873 K and a base pressure of 3.5×10^{-9} Torr, followed by *in situ* annealing at 973 K for 1 h. No oxygen gas flow was introduced during growth and annealing. The thickness of the measured films was about 650 nm. Hall measurements were performed using the Van der Pauw configuration (Bio-Rad Microscience HL5500 Hall System) at 296 K and yielded a background electron concentration of 2.87×10^{16}–7.06×10^{18} cm^{-3} with a mobility of 28.2–40.9 cm^2 V^{-1} s^{-1} and resistivity of 0.771–0.0216 Ω cm. XRD measurements were performed with an eight-circle diffractometer at the wiggler beamline BL17B of the National Synchrotron Radiation Research Center (NSRRC) with incident wavelength 1.1808 Å. Two pairs of slits located between the sample and an NaI scintillation detector were employed and yielded a typical resolution of better than 4×10^{-4} nm^{-1}. In terms of line width analysis, the full width at half-maximum (FWHM) of each reflection was obtained by fitting the measured data with a pseudo-Voigt function, which is a combination of Gaussian and Cauchy functions (Keijser *et al.*, 1982). Finite crystallite size and inhomogeneous strain are known as the two major sources of diffraction peak broadening. Line width broadening due to the former is independent of the diffraction order, whereas broadening due to the later is proportional to the diffraction order. We thus employed a Williamson–Hall plot (Williamson & Hall, 1953), which takes advantage of the mentioned different dependence of the line width broadening on the scattering order to discriminate between the two effects. For microscopic measurements, a cross-sectional TEM sample with a thickness of about 90 (10) nm was prepared by focused ion beam (FIB) techniques, and the TEM images were taken with a Philips TECNAI-20 field-emission-gun-type microscope by MA Tech. Inc. A commercial closed-loop-scanner scanning probe microscope (SPM; Digital Instruments 3100) with Ti/Pt-coated cantilevers (MikroMasch) was adopted for surface morphology and local electrical property measurements. For the SCM measurements, V_{ac} (2 V) and V_{tip} (2 V) were applied.

3. Results and discussion

3.1. XRD

Radial (2θ–ω) scans along the surface normal were conducted and only the 000*l* reflections of both sapphire and ZnO were observed, elucidating the *c*-plane orientation of the grown ZnO layers. Azimuthal cone scans (φ scans) across the off-normal ZnO $\{20\bar{2}2\}$ and sapphire $\{20\bar{2}2\}$ peaks, as illustrated in Fig. 1(*a*), were measured to examine the in-plane epitaxial relation. Six ZnO diffracted peaks (FWHM $\simeq 0.57^\circ$) that are evenly spaced 60° apart confirm that the ZnO film has sixfold rotational symmetry against the surface normal and is grown epitaxially on the *c*-plane sapphire. The 30° offset between the $\{20\bar{2}2\}$ reflections of ZnO and sapphire verifies the in-plane epitaxial relationship of $[10\bar{1}0]_{sapphire} \parallel [11\bar{2}0]_{ZnO}$ and $[11\bar{2}0]_{sapphire} \parallel [01\bar{1}0]_{ZnO}$.

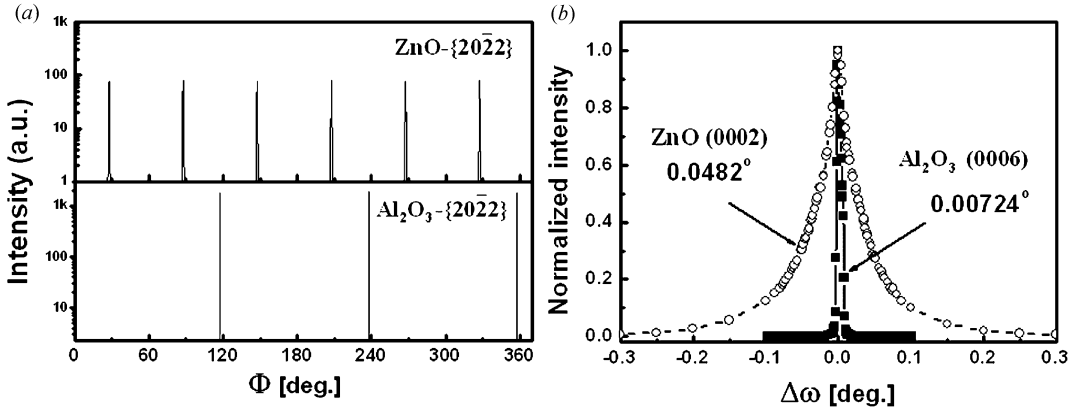

Figure 1
(*a*) Azimuthal scans of ZnO $\{20\bar{2}2\}$ and sapphire $\{20\bar{2}2\}$ peaks. (*b*) Comparison of ω scans of ZnO 0002 and substrate sapphire 0006 peaks. (All marked values denote FWHM.)

To characterize the structural quality of the grown films, the ω rocking curve of the ZnO 0002 reflection, as shown in Fig. 1(*b*), was measured. The rocking curve of the nearly resolution-limited sapphire 0006 reflection is also shown as a reference. The narrow width, 0.0072°, of the sapphire 0006 reflection reveals that the contribution of instrumental broadening to the ZnO width is negligible. The obtained mosaic spread of the ZnO film, 0.0482°, is much smaller than other reported values, typically ~0.2°, of ZnO films prepared with PLD (Vispute *et al.*, 1997; Fouchet *et al.*, 2004). It is also noticed that the line widths of the ZnO specular 0002 and off-normal $\{20\bar{2}2\}$ reflections are different by more than an order of magnitude. Such a prominent difference of diffraction features in these two groups reveals the structural characteristics of the films.

TDs in a film produce crystalline plane distortions and the associated lattice deformation depends on the geometry of the TDs (Heying *et al.*, 1996). For a *c*-plane ZnO layer, TDs with their dislocation lines lying along the [0001] direction, *i.e.* normal to the ZnO/sapphire interface, are most often observed (Vigué *et al.*, 2001; Lim *et al.*, 2001). In our case, the majority of TDs have their lines along the [0001] direction, which will be discussed in more detail in §3.2. For a (0001)-oriented thin film with wurtzite structure, the TDs are classified into three different types according to the direction of the corresponding Burgers vector (**b**) relative to the [0001] line direction. They are edge dislocation with $\mathbf{b}_E = \langle 11\bar{2}0\rangle/3$, screw dislocation with $\mathbf{b}_C = \langle 0001\rangle$ and mixed dislocation with $\mathbf{b}_M = \langle 11\bar{2}3\rangle/3$, which is a combination of $\mathbf{b}_E$ and $\mathbf{b}_C$. Pure edge TDs twist the surrounding ZnO lattice about [0001], leading to the formation of vertical grain boundaries (Ponce, 1998; Vigué *et al.*, 2001; Chierchia *et al.*, 2003). Under this circumstance, the (*hkil*) crystalline planes with nonzero in-plane component, *i.e.* either *h* or *k* is not zero, are distorted. On the other hand, the pure screw TDs result in the tilting of the ZnO lattice, generating a pure shear strain field (Strikant *et al.*, 2002), and the crystalline planes with nonzero *l* are deformed. Therefore, to investigate the influence of edge TDs, we measured the profiles of $h0\bar{h}0$ surface reflections, which are not sensitive to lattice distortion caused by pure screw TDs. Such scans were performed in the grazing incidence diffraction geometry by keeping the surface normal almost perpendicular to the vertical scattering plane. The FWHM values of ω rocking curves reflect the lattice twist, and the widths of radial scans yield the lateral strain field and domain size. As a complement, we also measured the line widths of the 000*l* normal reflections, which are not affected by the pure edge TDs. The ω rocking curves and radial scans provide the lattice tilt angle and coherence size as well as the strain profile along the surface normal.

Fig. 2(*a*) displays the intensity distribution of scattered X-rays along the radial scans across the ZnO 0002 and $10\bar{1}0$ reflections, of which the former is along the growth direction and the latter lies on the sample surface. The FWHM of the former, 0.00816 nm^{-1}, is significantly smaller than that of the latter, 0.01565 nm^{-1}, indicating that the strain along the surface normal caused by screw TDs is much smaller than that along the lateral direction caused by edge TDs. The profiles of ω rocking scans across the ZnO 0002 and $10\bar{1}0$ reflections are illustrated in Fig. 2(*b*). Similarly, the FWHM of the 0002 reflection, 0.048°, is much smaller than that of the $10\bar{1}0$ reflection, 0.578°, revealing the tilt angle to be smaller than the twist angle. This pronounced difference of widths between the 0002 and $10\bar{1}0$ reflections strongly indicates that the density of pure edge TDs is greater than that of pure screw TDs. These observations are qualitatively similar to what was observed for GaN grown on *c*-plane sapphire (Heying *et al.*, 1996; Metzger *et al.*, 1998). The analogous phenomena are attributed to the similar crystal structures of ZnO and GaN, both belonging to space group $P6_3mc$, and the similar lateral lattice parameter, with a difference of ~1.8%.

To obtain meaningful quantitative results, we employed a Williamson–Hall plot (Δq_r *versus* q, with $q = 2\sin\theta/\lambda$ denoting the scattering vector and Δq_r the line width in q along the radial direction) to separate the broadening due to finite structural coherence length from strain-induced broadening. The inverse of the ordinate intercept yields the coherence length, *i.e.* the effective domain size, and the slope yields the r.m.s. inhomogeneous strain averaged over the effective domains (Williamson & Hall, 1953). Fig. 3(*a*) illustrates the

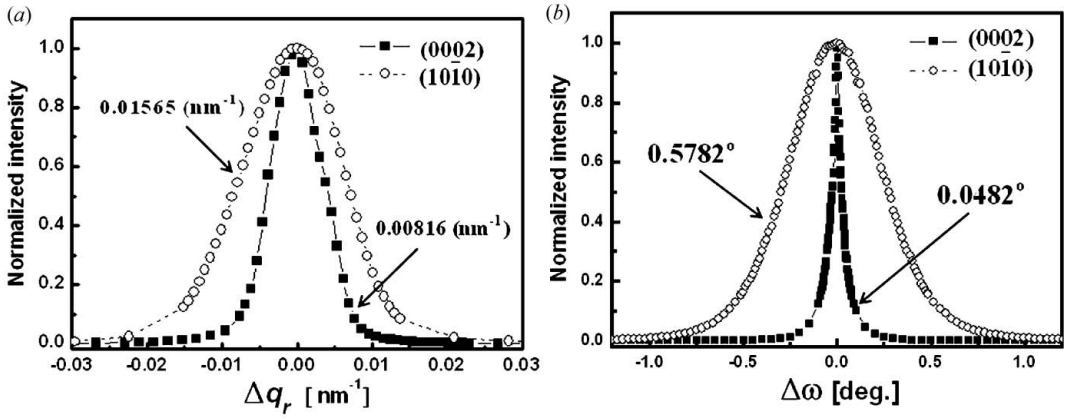

Figure 2
Superimposed radial (*a*) and symmetric ω scans (*b*) of ZnO 0002 and $10\bar{1}0$ reflections. The abscissa of (*a*), Δq_r, is the deviation of the scattering vector, $q = 2\pi\sin(\theta)/\lambda$, away from the corresponding reflection in the radial direction. (All values denote FWHM.)

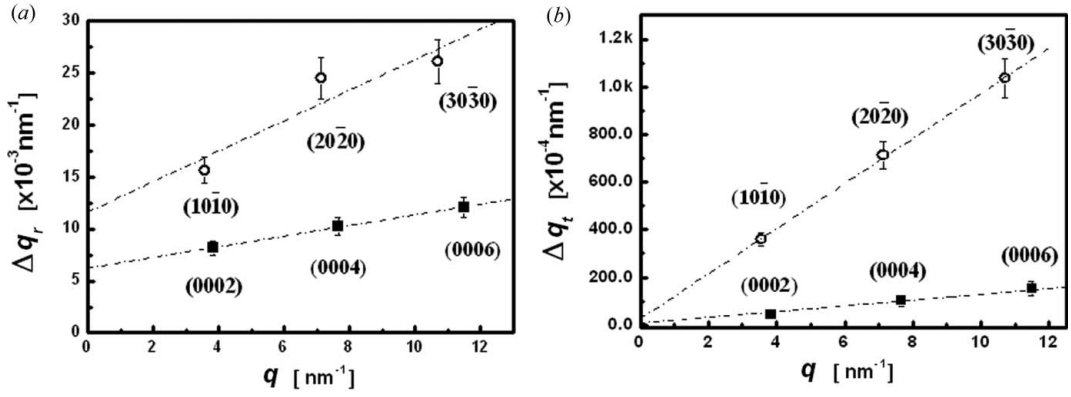

Figure 3
Williamson–Hall plots for a ZnO layer of radial scans (*a*) and ω rocking curves (*b*). The symmetric radial scans and ω rocking curves were measured for the 000*l* and *h*0$\bar{h}$0 reflections as indicated in the figures. Dashed lines are linear fits of the data.

Williamson–Hall plot of radial scans along the ZnO 000*l* and *h*0$\bar{h}$0 reflections. The correlation lengths obtained are 159.8 nm along the surface normal, which is only a fraction of the film thickness, and 86.1 nm along the lateral direction. The average lateral strain is 1.49×10^{-3}, about three times that along the surface normal, 0.51×10^{-3}, manifesting edge dislocations to be the dominant cause of distortion of the ZnO lattice. Analogous to the Williamson–Hall plot for radial scans, Fig. 3(*b*) shows a Δq_t *versus* q plot (where $\Delta q_t = \Delta\omega\, q$, denoting the line width in q along the transverse direction) for ω scans across the 000*l* and in-plane *h*0$\bar{h}$0 reflections, of which the slopes yield the spreads of tilt and twist angle, respectively. The obtained tilt angle ($\alpha_\Omega = 0.089^\circ$) is only one-sixth of the twist angle ($\alpha_\Phi = 0.542^\circ$). The densities of screw and edge TDs can be evaluated, respectively, from the corresponding Burgers vector and the tilt/twist angle. For screw TDs, the density N_S is calculated according to $N_S = \alpha_\Omega^2/(4.35 b_C^2)$ (Gay *et al.*, 1953), where α_Ω is the tilt angle and b_C denotes the length of the corresponding Burgers vector $\mathbf{b}_C$, which is [0001] with $b_C = 0.5225$ nm in this case. Applying the values determined from XRD, we obtained $N_S = 2.03 \times 10^8$ cm^{-2}. For edge TDs, the formula employed to calculate the density, N_E, depends on the spatial arrangement of the TDs (Hordon & Averbach, 1961). Assuming a random distribution, we apply $N_E = \alpha_\Phi^2/(4.35 b_E^2)$, in which α_Φ denotes the twist angle. In the case of TDs accumulating at a small-angle boundary, we adopt the formula $N_E = \alpha_\Phi/(2.1|b_E|L)$, where L denotes the correlation length along the in-plane direction. In both formulae of N_E, b_E is the length of associated Burgers vector $\mathbf{b}_E = \langle 11\bar{2}0\rangle/3$ (0.3238 nm). The edge TD densities for a random distribution and for accumulation at small-grain boundaries so obtained are 2.00×10^{10} and 1.62×10^{10} cm^{-2}, respectively. Even though the authentic distribution of edge TDs is uncertain, we expect it to be between a random distribution and an accumulation at a small-angle grain boundary, and the density N_E to be of the order of 10^{10} cm^{-2}. The results indicate that N_E is about 100 times higher than N_S; hence edge TDs are indeed the dominant type of dislocations in ZnO films grown on *c*-plane sapphire, in agreement with the conclusion drawn from a qualitative comparison of the FWHM values of the 0002 and 10$\bar{1}$0 reflections.

In a further examination of these results, we measured the radial scan profile of an off-normal 10$\bar{1}$4 reflection, of which both edge and screw TDs contribute to the line width broadening. The radial scan measured in an asymmetrical geometry is displayed in Fig. 4. The obtained width was compared with the calculated value by using the characteristic parameters of the edge and screw TDs, respectively, determined from *h*0$\bar{h}$0 and 000*l* reflections. The mean square strain of the (10$\bar{1}$4) planes induced by three edge dislocation systems with $\mathbf{b}_E = \langle 11\bar{2}0\rangle/3$ and slip planes $\{1\bar{1}00\}$ and the screw dislocation with $\mathbf{b}_C = \langle 0001\rangle$ can thus be calculated using the TD density obtained above ($N_E = 1.62 \times 10^{10}$ cm^{-2} and $N_S = 2.03 \times 10^8$ cm^{-2}) (Metzger *et al.*, 1998). The strain broadening of the 10$\bar{1}$4 Bragg reflection in the radial direction is subsequently calculated on the basis of such strain fields to yield an average of 0.078°. This value is in good agreement with the measured one (0.074°).

3.2. TEM

TEM contrast analysis was also performed to characterize the nature of the TDs. On the basis of the invisibility criterion, $\mathbf{g}\cdot\mathbf{b} = 0$, where $\mathbf{g}$ denotes the diffraction vector, the dislocations with Burgers vector $\mathbf{b}$ perpendicular to the diffraction vector $\mathbf{g}$ are invisible in the images. We thus took bright-field

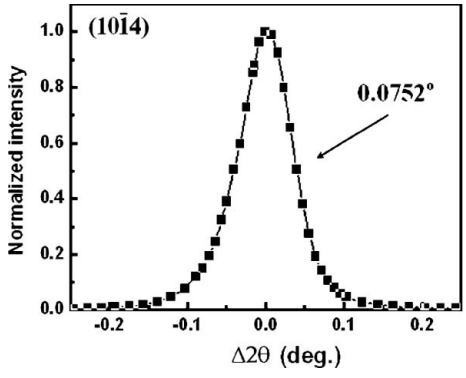

Figure 4
The profile of a radial scan across the ZnO 10$\bar{1}$4 reflection measured in an asymmetric geometry.

cross-sectional TEM images under a two-beam contrast condition with the zone axis near $[10\bar{1}0]$ and diffraction vectors **g** equal to (0002), $(11\bar{2}0)$ and $(11\bar{2}2)$, as shown in Figs. 5(*a*), 5(*b*) and 5(*c*), respectively. Pure edge TDs with $\mathbf{b}_E = \langle 11\bar{2}0\rangle/3$ are invisible in images recorded with **g** = (0002) but are in contrast in images with **g** = $(11\bar{2}0)$ and $(11\bar{2}2)$. Conversely, pure screw TDs with $\mathbf{b}_C = \langle 0001\rangle$ are out of contrast in the **g** = $(11\bar{2}0)$ case and are visible as **g** = (0002) and $(11\bar{2}2)$. As to the TDs of mixed type with $\mathbf{b}_M = \langle 11\bar{2}3\rangle/3$, they are visible in all three images. In all three micrographs, TDs seen as dark lines stem from the ZnO/sapphire interface with their dislocation lines primarily along the [0001] direction. The number of TDs is significantly less in Fig. 5(*a*) than in Figs. 5(*b*) and 5(*c*), manifesting that only a small fraction of TDs belong to pure screw type. Taking the specimen thickness of 90 (10) nm into account, we calculated the densities of edge, screw and mixed TDs to be approximately 1.5 (2) $\times 10^{10}$ cm^{-2} (~77%), 4.3 (3) $\times 10^{8}$ cm^{-2} (~2%) and 4.1 (5) $\times 10^{9}$ cm^{-2} (~21%), respectively. Thus 98% of the total TDs contain the edge component as determined from the TEM measurements.

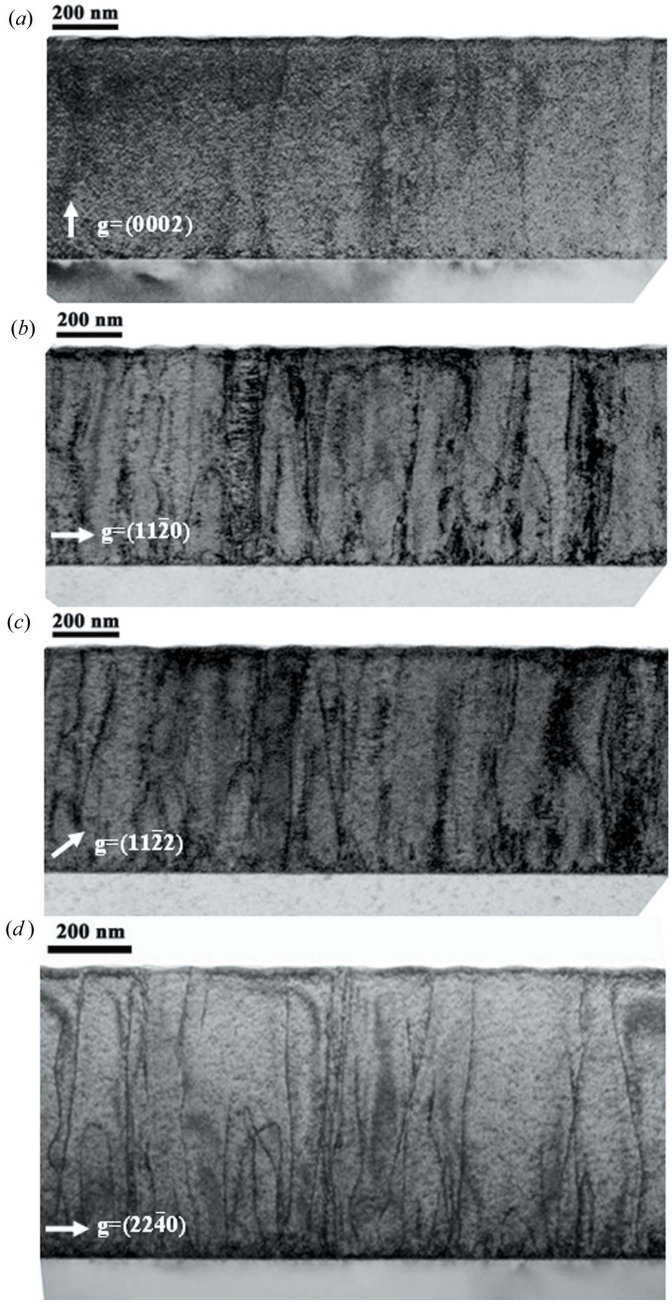

Figure 5
Two-beam bright-field cross-sectional electron micrographs of a ZnO thin film with **g** = (0002) (*a*), $(11\bar{2}0)$ (*b*) and $(11\bar{2}2)$ (*c*). Image (*d*) with **g** = $(22\bar{4}0)$ was taken at a region with particularly high TD density, in which several half loops were clearly identified.

In some regions, as shown in Fig. 5(*d*), the merging of dislocation lines to form half loops was observed, especially in the bottom half of the film close to the interface, revealing the strong interaction between the TDs. It appears that the annihilation of two nearby dislocations of opposite Burgers vectors leads to the formation of these loops. The presence of many half loops and the difference of TD density with depth may explain the smaller vertical structural coherence length found in XRD measurements as compared with the film thickness.

By tilting the specimen about the growth direction, we found that the diameters of columnar grains varied between 50 and 150 nm. After careful analysis, we obtained a mean diameter of 94 nm and a FWHM of 56 nm in lateral size distribution. Small-angle grain boundaries were also observed during the TEM measurement by tilting the sample about 0.6°, which is comparable to the FWHM (0.58°) of the azimuthal scan across the ZnO $\{20\bar{2}2\}$ reflections. From the TEM images, we found that the pure TDs are not uniformly distributed in the film but aggregate and encircle epitaxial ZnO cores. The structure of the ZnO layer is thereby described as a columnar-grain structure consisting of epitaxial cores and small-angle grain boundaries (annular regions) with edge TDs at a large density.

3.3. AFM/SCM

Figs. 6(*a*) and 6(*b*) show the AFM topography and SCM (dC/dV) images concurrently acquired with a V_{tip} of 2 V. The charge carriers of the ZnO film are in the accumulation condition under a tip bias of 2 V, because ZnO is an intrinsic n-type semiconductor. Therefore, a higher dC/dV signal level means a higher density of interface traps (D_{it}) and a lower free carrier concentration. The features observed in the two images are clearly mutually correlated. The hexagonal domains are clearly resolved in Fig. 6(*b*); the lateral domain size of about 86 nm is comparable to that obtained with XRD and TEM. Fig. 6(*c*) shows the dual-section profiles recorded along the line marked with arrows in both images to illustrate the correlation between the topography and the SCM signals. Comparing with the structural information obtained from XRD and TEM measurements, we ascribed the yellow circumferential curves and red regions to grain boundaries and epitaxial cores, respectively. We exclude the possibility that the contrast in the capacitance signal resulted from a topographic effect because the SCM contrast varied with tip bias [the stripe near the top of Fig. 6(*b*) with dim contrast was

recorded with V_{tip} = 1 V] and the r.m.s. roughness is small, about 0.25 nm. The contrast of AFM and SCM images is opposite, *i.e.* the annular region has a higher SCM signal level. We believe that TDs would introduce deep acceptor-like trap states in ZnO films and consequently increase D_{it} in the annular region, because the flat-band voltage shifts in dC/dV *versus* V_{tip} curves between the epitaxial core and TD region (Liu *et al.*, 2006). This SCM result agrees with the charge density distribution around the dislocation cores reported by Müller *et al.* (2006), who measured the electrostatic potential in the vicinity of charged dislocations by employing electron holography in a transmission electron microscope and derived the charge density accordingly. Since wurtzite ZnO has a high piezoelectric constant, it is possible that part of the charges observed by SCM could be piezoelectric (bound) charges at the surface, generated by the strain field of the dislocations (Shi *et al.*, 1999). However, Müller *et al.* (2006) estimated that the magnitude of piezoelectric charges in the dislocations is insignificant compared with that of charges in the dislocations. Therefore, we suggest that D_{it} is the major component of dislocation charges in ZnO. Although the main defect structures in the epitaxial ZnO and GaN films grown on *c*-plane sapphire substrates are both edge TDs, it is interesting to find out that the defect structures exhibit a distinct influence on the electrical properties of these films. For example, the edge TDs induce negative fixed charges in GaN films (Hansen *et al.*, 1998) but mainly generate interface trap density in ZnO films.

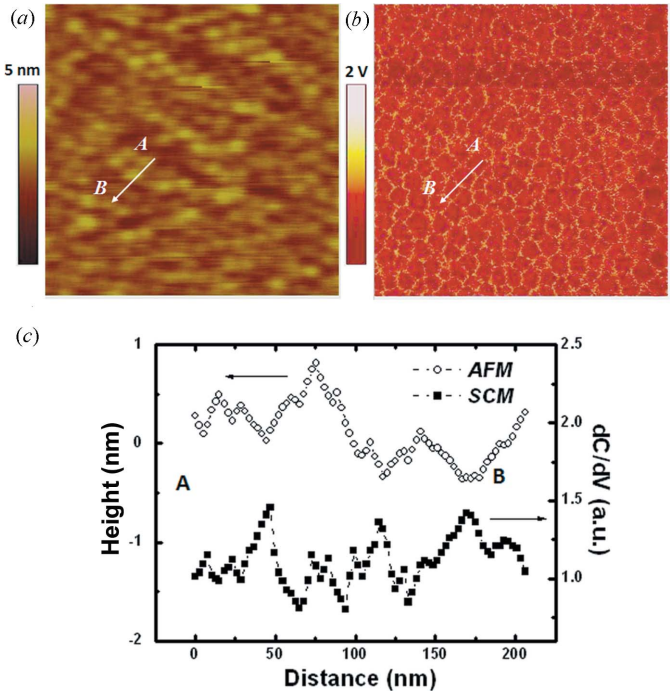

Figure 6
AFM topography (*a*) and SCM differential capacitance (dC/dV) image (*b*) of a ZnO film of area 1 × 1 µm acquired at V_{tip} = 2 V. The region near the top with dim contrast in (*b*) was acquired at V_{tip} = 1 V. (*c*) A dual-section profile recorded along the line indicated from *A* to *B* by arrows in (*a*) and (*b*).

4. Conclusions

Our XRD, TEM, AFM and SCM measurements on epitaxial ZnO films grown by PLD on *c*-plane sapphire substrates reveal that the predominant defect structures are edge TDs. These TDs are not uniformly distributed in the ZnO layer but aggregate to form annular regions around columnar epitaxial cores. The correlation between edge TDs and SCM mapping indicates that edge TDs introduce interface trap densities in the annular region. The large interface trap density increases the scattering of charge carriers, reduces the carrier mobility and accordingly degrades the performance of electro-optical devices. To reduce effectively TD density is still an important issue in the future applications of ZnO thin films.

We thank Mr C. M. Huang of NSRRC for assistance with X-ray diffraction measurements, and the Nanotechnology Research Center in the Industrial Technology Research Institute for access to the scanning capacitance microscope. The National Science Council (NSC) of Taiwan partially supported this work under contracts NSC-95-2112-M-213-005 and NSC-94-2112-M-029-004. W-RL acknowledges provision by the NSC of a fellowship under contract NSC-93-2112-M-213-006.

References

Bagnall, D. M., Chen, Y. F., Zhu, Z., Yao, T., Koyama, S., Shen, M. Y. & Goto, T. (1997). *Appl. Phys. Lett.* **70**, 2230–2232.
Chierchia, R., Böttcher, T., Heinke, H., Einfeldt, S., Figge, S. & Hommel, D. (2003). *J. Appl. Phys.* **93**, 8918–8925.
Fouchet, A., Prellier, W., Mercey, B., MéChin, L., Kulkarni, V. N. & Venkatesan, T. (2004). *J. Appl. Phys.* **96**, 3228–3233.
Gay, P., Hirsch, P. B. & Kelly, A. (1953). *Acta Metall.* **1**, 315–319.
Hansen, P. J., Strausser, Y. E., Erickson, A. N., Tarsa, E. J., Kozodoy, P., Brazel, E. G., Ibbetson, J. P., Mishra, U., Narayanamurti, V., DenBaars, S. P. & Speck, J. S. (1998). *Appl. Phys. Lett.* **72**, 2247–2249.
Heying, B., Wu, X. H., Keller, S., Li, Y., Kapolnek, D., Keller, B. P., DenBaars, S. P. & Speck, J. S. (1996). *Appl. Phys. Lett.* **68**, 643–645.
Hordon, H. J. & Averbach, B. L. (1961). *Acta Metall.* **9**, 237–246.
Hsu, J. W. P., Manfra, M. J., Molnar, R. J., Heying, B. & Speck, J. S. (2002). *Appl. Phys. Lett.* **81**, 79–81.
Keijser, Th. H. de, Langford, J. I., Mittemeijer, E. J. & Vogels, A. B. P. (1982). *J. Appl. Cryst.* **15**, 308–314.
Krivoglaz, M. A. (1996). Editor. *X-ray and Neutron Diffraction in Non-Ideal Crystals*. Berlin: Springer.
Lim, S. H., Washburn, J., Liliental-Weber, Z. & Shindo, D. (2001). *J. Vac. Sci. Technol. A*, **19**, 2601–2603.
Liu, W. R., Hsieh, W. F., Hsu, C.-H., Liang, K. S. & Chien, F. S.-S. (2006). *J. Cryst. Growth*, **297**, 294–299.
Metzger, T., Höpler, R., Born, E., Ambacher, O., Stutzmann, M., Stömmer, R., Schuster, M., Göbel, H., Christiansen, S., Albrecht, M. & Strunk, H. P. (1998). *Philos. Mag. A*, **77**, 1013–1025.
Miller, E. J., Schaadt, D. M., Yu, E. T., Poblenz, C., Elsass, C. & Speck, J. S. (2002). *J. Appl. Phys.* **91**, 9821–9826.
Müller, E., Gerthsen, D., Brückner, P., Scholz, F., Gruber, Th. & Waag, A. (2006). *Phys. Rev. B*, **73**, 245316.
Narayan, J. & Larson, B. C. (2003). *J. Appl. Phys.* **93**, 278–285.
Ng, H. M., Doppalapudi, D., Moustakas, T. D., Weimann, N. G. & Eastman, L. F. (1998). *Appl. Phys. Lett.* **73**, 821–823.

Ponce, F. A. (1998). *Group III Nitride Semiconductor Compounds: Physics and Applications*, edited by B. Gil, pp. 123–157. Oxford: Clarendon.
Shi, C., Asbeck, P. M. & Yu, E. T. (1999). *Appl. Phys. Lett.* **74**, 573–575.
Strikant, V., Speck, J. S. & Clarke, D. R. (2002). *J. Appl. Phys.* **82**, 4286–4295.
Sugahara, T., Sato, H., Hao, M., Naoi, Y., Tottori, S., Yamashita, K., Nishino, K., Romano, L. T. & Sakai, S. (1998). *Jpn. J. Appl. Phys.* **37**, L398–L400.
Tsukazaki, A., Ohtomo, A., Onuma, T., Ohtani, M., Makino, T., Sumiya, M., Ohtani, K., Chichibu, S. F., Fuke, S., Segawa, Y., Ohno, H., Koinuma, H. & Kawasaki, M. (2005). *Nat. Mater.* **4**, 42–46.
Vigué, F., Vennéguès, P., Vézian, S., Laügt, M. & Faürie, J.-P. (2001). *Appl. Phys. Lett.* **79**, 194–196.
Vispute, R. D., Talyansky, V., Trajanovic, Z., Choopun, S., Downes, M., Sharma, R. P., Venkatesan, T., Woods, M. C., Lareau, R. T., Jones, K. A. & Iliadis, A. A. (1997). *Appl. Phys. Lett.* **70**, 2735–2737.
Williamson, G. K. & Hall, W. H. (1953). *Acta Metall.* **1**, 22–31.